# Highly stretchable and sensitive SBS/Gr/CNTs fibers with hierarchical structure for strain sensors

Mengsi Liu [a, 1], Yaping Sheng [a, 1], Chenggang Huang [a], Yanfen Zhou [a, *], Liang Jiang [a,*], Mingwei Tian [a], Shaojuan Chen [a], Stephen Jerrams [b], Fenglei Zhou [c], Jianyong Yu [d]

[a] College of Textiles and Clothing, Qingdao University, Qingdao 266071, China

[b] Centre for Elastomer Research, FOCAS, Technological University Dublin (TU Dublin), City Campus, Kevin St, Dublin D08 NF82, Ireland

[c] Centre for Medical Image Computing, University College London, London, WC1V 6LJ, UK

[d] Innovation Center for Textile Science and Technology, Donghua University, Shanghai, 200051, China

---

[*] Corresponding authors. E-mail: liang.jiang@qdu.edu.cn (Liang Jiang); yanfen.zhou@qdu.edu.cn (Yanfen Zhou).

[1] Mengsi Liu and Yaping Sheng contributed equally to this work.

**Abstract**

Most of the reported flexible strain sensors can only normally sense external stretch in a quite narrow working range and with low sensitivity. In order to overcome these drawbacks, elastomeric fiber based strain sensors incorporating graphene (Gr) and carbon nanotubes (CNTs) were initially fabricated via coaxial wet spinning. The solution etching method was employed for forming a 1D@2D@1D hierarchical structure, with pores and microcracks on fibers, to reconstruct their conductive networks. The solution etched fiber based strain sensors achieved a significant improvement in obtaining a high maximum gauge factor of 1667 and capability of working over a wide strain range (0-500%, approximately 31 times larger than that for the non-etched fiber). Furthermore, the strain sensor showed excellent durability over 10000 tensile strain cycles. Finally, the based strain sensor was used to monitor physiological movements such as finger, elbow and knee bending with fast and accurate responses.

**Keywords:** Strain sensor; Carbon nanotubes; Graphene; Wet-spinning; Fibers.

## 1. Introduction

In recent years, wearable electronics with high stretchability and flexibility have been extensively used in various fields, such as electronic skins, artificial intelligence, energy storage devices and human-motion strain sensors[1-4]. Among them, strain sensors that can transform mechanical deformations into electrical signals have attracted considerable attention because of their potential to find various applications in human motion monitoring, health monitoring and human-machine interface technology [5-7]. However, despite their high sensitivity, traditional strain sensors prepared from metals and semiconductor materials are usually rigid and suffer from poor extensibility (below 200%) [8].

In contrast, conductive polymer composites (CPCs) are regarded as good candidates for fabricating strain sensors due to their good flexibility and extensibility [9]. Commonly used methods of obtaining CPCs include depositing conductive fillers (such as carbon nanotubes (CNTs), graphene (Gr), carbon black (CB), carbon nanofiber (CNF), $Ti_3C_2T_x$ (MXene), copper nanoparticles and Ag nanowires (AgNWs) on the surface of flexible polymers [2, 5, 10-13], and directly incorporating these conductive fillers into flexible polymer matrices [14, 15]. The coating layer of those CPCs are prone to being easily detached, significantly affecting their electrical properties and long-term stability [16]. By comparison, incorporating conductive fillers into polymer matrices has the advantages of achieving superior combination between fillers and matrices, and providing stable electrical properties after washing and friction [17, 18]. However, CPCs based strain sensors do not easily achieve wide working ranges due to the destruction of conductive pathways they experience under large deformations. It has been reported that the electrical performance of strain sensors can be varied by changing their shape and the concentration

and distribution of the conductive fillers to form different conductive networks [19, 20]. Furthermore, when incorporating the mixture of 1D CNTs and 2D Gr sheets into matrices [21-23] , an effective and stable conductive network can be formed. This improvement is mainly ascribed to the synergistic effect between Gr and CNTs. CNTs possessing a high length to diameter ratio have the ability to bridge the isolated Gr sheets, which have high specific surface areas, to form efficient conductive networks in the matrices [24, 25]. However, the increase in the extensibility of the strain sensors is still relatively small, over a low working range of approximately 90%.

In CPCs, forming a conductive path is greatly impeded by the insulated matrices around the conductive fillers[26, 27]. Also, the conductive path is usually fragile and hence easily broken during stretching [13, 28]. In order to overcome these drawbacks, endeavor has been made to achieve high sensitivity and large working strain ranges for the materials by creating crack structures in accordance with microcrack theory [25, 29-31]. This can be accomplished by stretching elastic polymers coated with brittle thin conductive layers. However, the generation of cracks is normally harmful to mechanical properties and the working range of the CPCs based on crack structure is still low [32, 33].

In this work, conductive fibers were initially fabricated by using flexible polystyrene-butadiene-styrene (SBS) matrices and Gr/CNTs hybrid fillers using wet spinning. The pure SBS solution was used as the core layer and SBS/Gr/CNTs solution was used as a sheath layer in order to obtain strain sensor with a further improved strain sensitivity and reduce its cost [34].

In particular, a solution etching-based method was proposed to remove the insulated polymer around Gr and CNTs on the surface of fibers to form pores and microcracks on the surface of fibers. Additionally, Gr and CNTs in the solution was implanted on the

surface of fibers to endow the composite fiber a 1D@2D@1D (CNTs@Gr@fiber) hierarchical structure. The conductive components shown on the surface of the substrate after etching were analogous to exposed reefs in the sea after an ebb tide. As a result, the exposed conductive fillers on the surface of the fibers were inclined and contacted as the composites deformed, leading to the formation of additional conductive paths. Concurrently, mechanical properties were maintained at a high level by controlling the etching time. The morphology, mechanical properties, electrical properties and sensing behaviors of the solution etched SBS/Gr/CNTs fibers (SSCGFs) were investigated. Thereafter, the working stability and durability of SSCGFs were further studied. Finally, a prototype of an SSCGF based strain sensor to detect human finger, elbow and knee bendings was proposed.

## 2. Experimental

### 2.1 Materials

SBS was purchased from SINOPEC Maoming Petrochemical Co., Ltd. (Guangdong, China). Multi-walled carbon nanotubes (CNTs), having tube diameters of 3-15 nm and tube lengths of 15-30 μm, and Gr with 1-3 layers were both purchased from Turing Evolution Technology Co., Ltd. (Shenzhen, China). Tetrahydrofuran (THF), N,N-Dimethylformamide (DMF), dichloromethane, ethyl acetate and anhydrous ethanol were provided by Sinopharm Chemical Reagents Co., Ltd. (Shanghai, China).

### 2.2 Preparation of SSCGF

The procedure for preparing SSCGFs is depicted in Figure 1(a). Firstly, both Gr and CNTs as fillers were added into THF and ultrasonicated for 2 h in order to obtain good dispersion. Then SBS pellets were added in the obtained suspension and magnetically stirred for 18 h at room temperature. Subsequently, pure SBS solution as the inner layer and

SBS/Gr/CNTs solution as the outer layer were each loaded into 20 ml syringes, which were connected with a coaxial needle (18G/25G) fixed on a syringe pump. Then, the solutions were injected into an ethanol coagulation bath to obtain SBS/Gr/CNTs fibers (SCGFs). The whole spinning process was carried out at ambient temperature with a solution injection speed of 10 mL/h. The resultant fibers were denoted as SBS/xGr/yCNTs, where x and y represent the weight percentage of Gr and CNTs in the composite fibers, respectively. Taking SBS/6Gr/1CNTs as an example, the mass ratio of Gr and CNTs in the composite fibers was 6.0 wt.% and 1.0 wt.%, respectively. The formation mechanism of SCGFs is illustrated in Figure 1(b). When the spinning solution entered the ethanol coagulation bath, a dense solidified skin immediately formed to cover the fluid core. Thereafter, the ethanol coagulation bath diffused into the freshly formed fluid filament, and THF as a solvent was transferred from the filament to the bath. Meanwhile, solidification interfaces were formed between the solidified parts and the non-solidified parts of the filament. With an increase in the immersion time of the filament in the coagulation bath, solidification interfaces slowly moved from surface to core. Finally, the fiber was completely formed.

The SCGFs obtained were etched with ethyl acetate mixed with Gr/CNTs at a ratio of 4:3 in order to repair the destroyed conductive paths and thereby forming a hierarchical structure with 1D CNTs and 2D Gr sheets embedded in the surface of 1D fibers during the dissolving process. These fibers were denoted as SSCGFs. As can be seen from Figure 1(c) and (d), the conductive fibers etched with pure solvent merely had a large amount of surface pores, while SSCGFs had pores and microcracks with Gr sheets and CNTs on their surfaces. This outcome was beneficial to the enhancement of electrical conductivity.
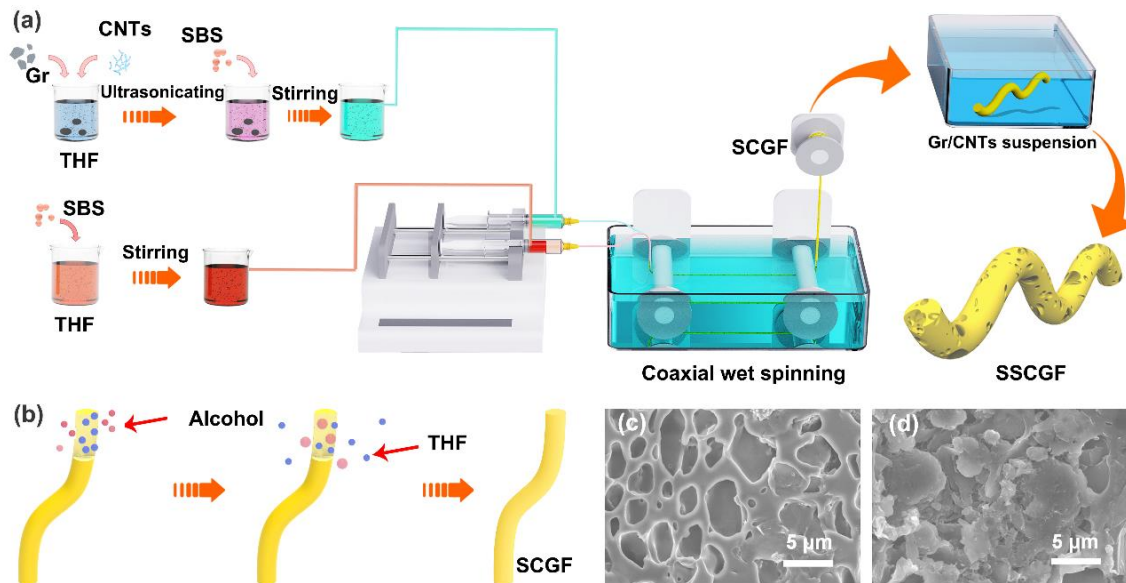
Figure 1 (a) Schematic of the preparation process of core-sheath SSCGFs; (b) Schematic of fiber forming during the wet spinning process; the SEM images of SCGF etched with (c) ethyl acetate only and with (d) ethyl acetate/Gr/CNTs.

## 2.3 Characterization

A scanning electron microscope (SEM, TESCAN VEGA3, Czech) was employed to observe the morphology of SCGFs and SSCGFs at an accelerated voltage of 10 kV. The mechanical properties of SSCGFs were determined using a universal tensile machine (Instron 5965, Glenview, USA) with a uniaxial tensile force applied at a feed rate of 100 mm/min. Raman spectra were obtained by employing a Raman microscope (Thermo Scientific DXR2, America). The thermogravimetric analysis was conducted using a DSC/TG synchronous thermal analyzer (STA449 F3 Jupiter, Bavaria, Germany) under a nitrogen atmosphere with a heating rate of 20 °C/min. Electromechanical properties were characterized by employing a digital multimeter (Keysight B2901A, Keysight Technology, USA) connected with a stepper motor to induce tensile deformations to the test samples.

## 3. Results and discussion

Electrically conductive SCGFs with different Gr/CNTs mass ratios were prepared through coaxial wet spinning. The morphology, mechanical properties and electrical conductivity of SCGFs are shown in the Supplementary material. Among these composite fibers, SBS/3Gr/4CNTs fibers exhibited uniform morphology, the highest electrical conductivity of $1.42 \times 10^{-3}$ S/cm and the highest elongation at break 1293.4% which ensures the possibility of reaching a large working strain range. Thus, it was adopted for surface etching and subsequent tests. The SBS/3Gr/4CNTs fibers before etching and after etching for 15s, 30s and 45s were denoted as SCGF, SSCGF-15, SSCGF-30 and SSCGF-45, respectively below. Figure 2(a)-(d) shows the surface morphology of SCGF, SSCGF-15, SSCGF-30 and SSCGF-45 respectively. It can be seen that Gr and CNTs were evenly dispersed in the SBS matrix for SCGF, while some of Gr and CNTs were observed on the surfaces of SSCGF-15, SSCGF-30 and SSCGF-45. Furthermore, it was found that more precipitated conductive fillers emerged on the surface of fibers forming a hierarchical structure when etched for longer times as shown in Figure 2(II′-VI′). Additionally, it can be seen from the cross-section morphology of the fibers (Figure 2(I-VI)) that all fibers had a faba bean shape. Gr and CNTs were fully embedded in the SBS, indicating a strong interaction and good interface compatibility among Gr, CNTs and SBS. This is due to strong π-π staking interactions between benzene ring in SBS macromolecules and ring structures were present in the Gr and CNTs [35, 36]. It can also be seen that both Gr and CNTs sheets were exposed on the surface of SSCGFs because the surrounding SBS layers were removed by solvent etching, leading to rough profile of the fibers.
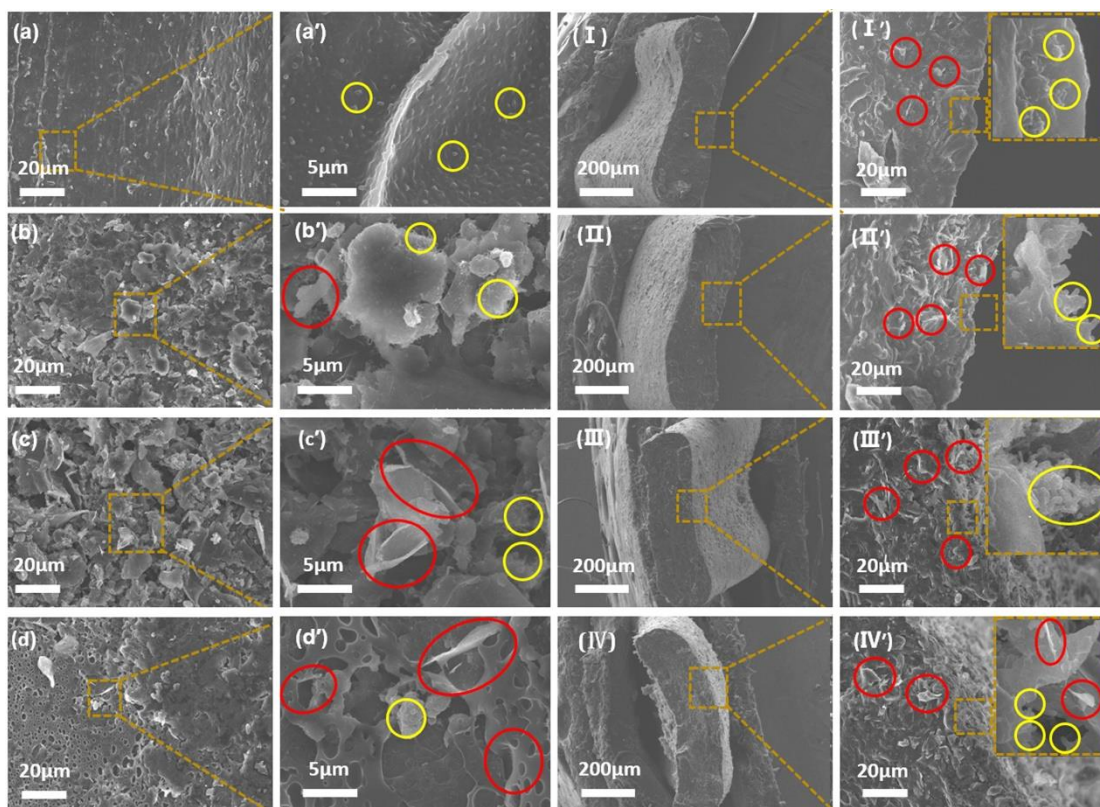
Figure 2 (a-d) Surface morphology of SBS/3Gr/4CNTs fibers after etching with ethyl acetate for 0s, 15s, 30s and 45s, respectively; (I-VI) depicts the corresponding cross-section morphologies. Conductive fillers including Gr and CNTs are marked with red and yellow circles, respectively.

Figure 3(a) shows the stress-strain curves of SCGF, SSCGF-15, SSCGF-30 and SSCGF-45. The SCGF fibers had a tensile strength of about 23.3 MPa and an elongation at break of about 1800%. When the fibers were treated with ethyl acetate/Gr/CNTs mixture for 15s, the elongation at break decreased to 1200% while the tensile strength decreased to about 21.2 MPa. With the increasing etching time up to 45s, the tensile strength decreased further. This can be explained in terms of two aspects: more SBS matrix was removed from the fibers by ethyl acetate subject to a longer etching time; during the solvent diffusion into the matrix, the oriented macromolecules formed by spinning were relaxed and the distance between adjacent molecules increased, resulting in a weakened

interaction [37], Additionally, it can be seen from Figure 3(d) that with increasing the etching time, the amount of SBS removed from the surface of fibers increased. Therefore these led to a reduction in tensile strength and elongation at break (as shown in Figure 3(b)) [38].

Raman spectroscopy was used to characterize the carbon structure for CNTs, Gr and SBS. Figure 3(c) shows that all SSCGFs had typical D-bands and G-bands at 1349 $cm^{-1}$ and 1581 $cm^{-1}$ respectively, indicating the existence of CNTs. The 2D-band present at 2698 $cm^{-1}$ confirmed the existence of the Gr structure. The peaks at 2918 $cm^{-1}$, which originated from C-H stretching of the SBS, became weaker after etching. When the etching time reached 45s, the peak at 2918 $cm^{-1}$ disappeared. These results manifested that ethyl acetate etching removed the SBS matrix from the fiber surfaces but had little effect on the structure of Gr and CNTs.

The quantity of Gr and CNTs in SSCGFs was measured by TG. As shown in Figure 3(d), the SCGF and SSCGFs started to decompose at about 280 °C. When the temperature reached 500 °C, the mass residue almost ceased to decrease. The residuals for the SCGF, SSCGF-15, SSCGF-30 and SSCGF-45 were 3.7%, 4.6%, 4.8% and 5.4%, respectively, suggesting an increase in remaining conductive filler with increased etching time for SSCGFs. This may have been instrumental in enhancing their conductivity.
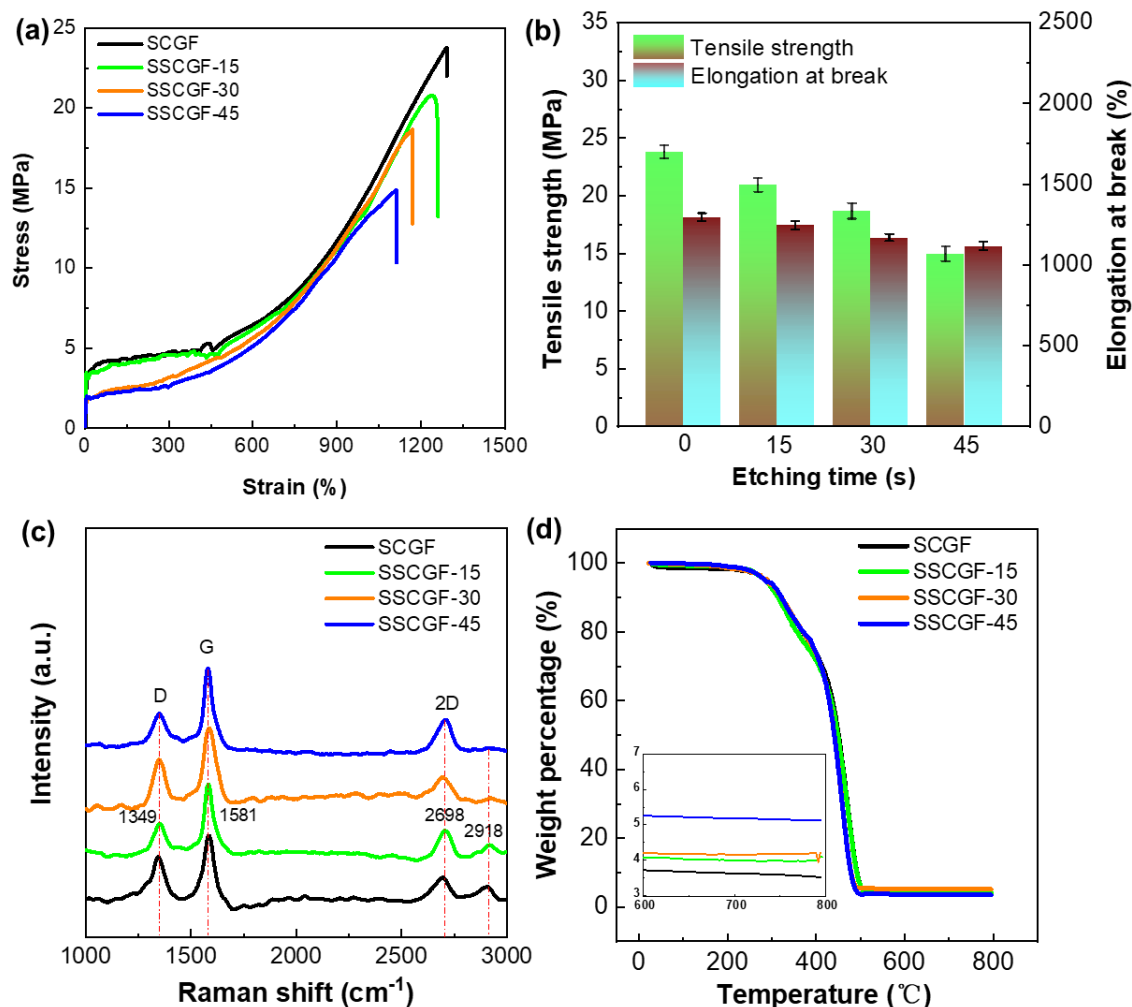
Figure 3 (a) Stress-strain curves, (b) Tensile strength and elongation at break, (c) Raman spectra and (d) TG curves of SCGF and SSCGFs.

Figure 4(a) shows the electrical conductivity of SCGF and SSCGFs. Compared with SCGF, the electrical conductivity of SSCGFs increased and SSCGFs-45 exhibited the highest conductivity of $1.69 \times 10^{-1}$ S/cm. This was probably because more conductive networks were constructed after the isolating SBS layers between the adjacent conductive fillers on the surface were removed by ethyl acetate.

Figure 4(b) shows the dependence of relative resistance change ($\Delta R/R_0$, where $\Delta R = R - R_0$, R is the real-time resistance and $R_0$ is the initial resistance) of SCGF and SSCGFs on tensile strain. The tensile feed rate was set at 5 mm/min. It was observed that $\Delta R/R_0$

increased with increasing strain for all samples. The SCGF without etching had a very narrow working range of 0-16%, whereas the strain sensing ranges of SSCGFs became significantly wider. Notably, the SSCGF-15 had a working range of 0-500% with a high gauge factor (GF = $(\Delta R/R_0)/\varepsilon$, where $\varepsilon$ is the applied strain) of 1667. The maximum sensing strain and GF were superior to the values for most recently reported strain sensors [2, 5-6, 8-11, 17, 20-24, 27-29, 35-36] (Figure 4(c)).

The experimental data of $\Delta R/R_0$ versus strain was subjected to curve fitting by using the theory associated with the "tunnel effect" [39-41] , which is expressed by Eq. (1).

$$\frac{\Delta R}{R_0} = \frac{R-R_0}{R_0} = \left(\frac{sN_0}{Ns_0}\right)\exp\left[\gamma(s-s_0)\right]-1 = (1+a\varepsilon)\exp\left[\left(A+\gamma as_0\right)\varepsilon+B\varepsilon^2+C\varepsilon^3+D\varepsilon^4\right]-1 \quad (1)$$

where $N$ is related to the number of conductive paths, $N_0$ is the quantity of conductive paths in the original state, $s$ refers the smallest distance between the adjacent conductive fillers, $s_0$ is the original distance between conductive fillers, and $a$, $A$, $B$, $C$, $D$ are constants.

As presented in Figure 4(b), the experimental data of SSCGF-15 was in good agreement with the theoretical values calculated from Eq. (1) with $R^2$ value of 0.9985. In order to investigate the electrically conductive stability of SSCGF-15, an ultrasonication water washing test for SSCGF-15 was carried out and the relationship between electrical resistance and washing time is shown in Figure 4(c). For the same sample, the conductivity decreased from $3.93\times10^{-2}$ S/cm to $2.84\times10^{-2}$ S/cm with increasing washing time up to 60 min and then almost stable thereafter.
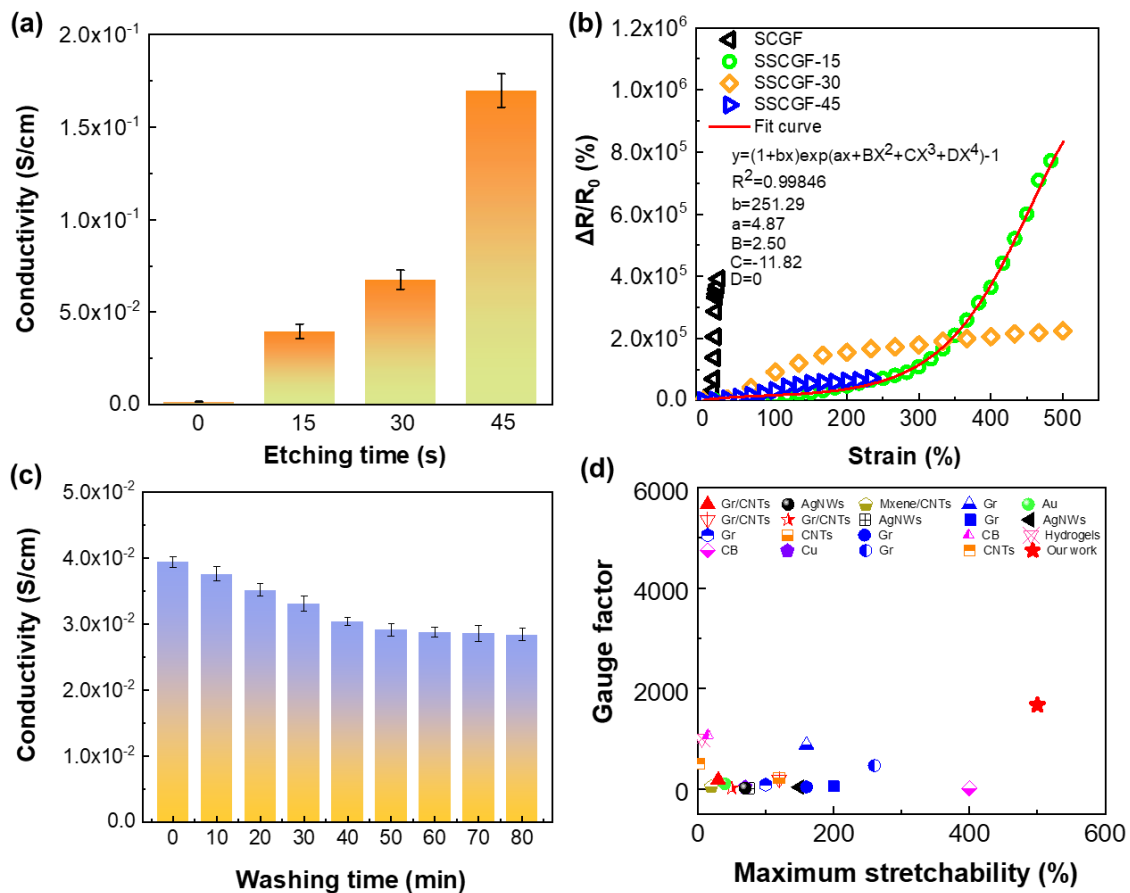
Figure 4 (a) Electrical conductivity of SSCGF obtained at different etching times; (b) $\Delta R/R_0$ versus strain curves for SCGF, SSCGF-15, SSCGF-30 and SSCGF-45; (c) Histogram of sheet resistance of SSCGF-15 after washing for different times; (d) Comparison of the maximum GF and the maximum sensing strain incorporated with different fillers, such as such as Gr [20, 22, 24, 35-36], CNTs [10, 23], Gr/CNTs [2, 9, 17], $Ti_3C_2T_x$ (Mxene)/CNTs [6], carbon black (CB) [27, 29], hydrogels [28], AgNWs [5, 18, 21], copper (Cu) [11] and gold (Au) [8], reported in the literature and SSCGF-15 in this work.

Figure 5 shows the surface morphology of SSCGF-15 unstretched and stretched to 150%, 300% and 500%. As can be seen from Figure 5(a), a large amount of pores and microcracks were formed on the surface of SSCGF having the hierarchical structure after etching, as mentioned previously. During extension, the dimensions of the pores and

microcracks became larger and more microcracks evolved from the pores (as shown in Figure 5(b)). Gr sheets and CNTs were clearly seen to be imbedded in the pores and microcracks as shown in Figure 5 (b'). With increasing tensile strain to 300%, large scale microcracks were clearly observed on the surface of the SSCGF as shown in Figure 5(c) and (c'). However, the fiber was elongated directly leading to the decrease of the density of pores and microcracks distributing on the fiber. When the tensile strain was up to 500%, more microcracks (shown in Figure 5(d) and (d')) were formed on the surface of fibers with stacked Gr sheets decorated with CNTs. These are beneficial for the enhancement of the electrical properties of SSCGF [42].
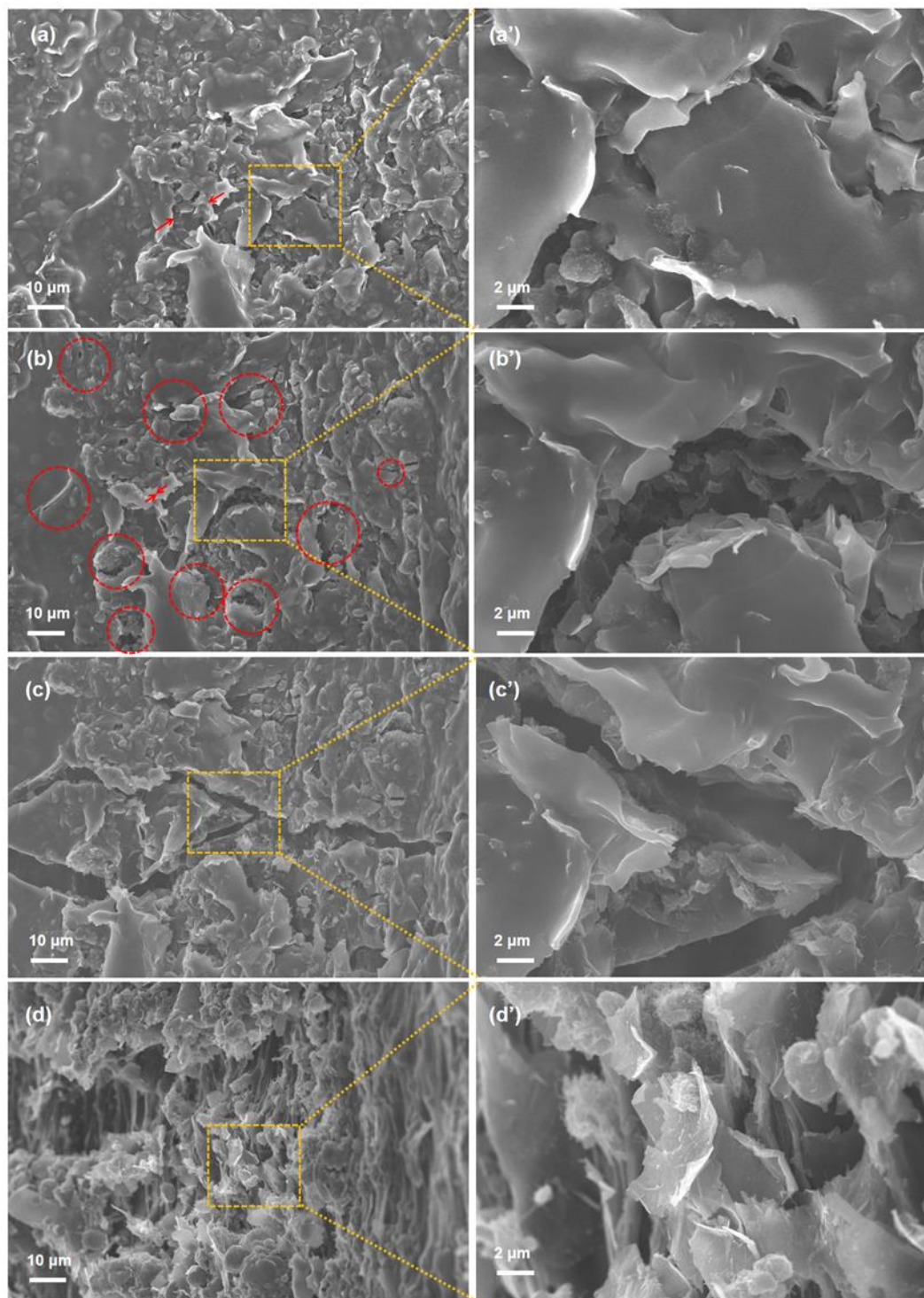
Figure 5 Surface morphology of SSCGF-15 unstrained (a, a'), with stretch ratios of 150% (b, b') 300% (c, c') and 500% (d, d').

The mechanism of achieving enhanced electrical conductivity and broader working ranges for the SSCGFs is illustrated schematically in Figure 6. For the coaxial wet spun

SCGF, Gr and CNTs were dispersed in the SBS matrix to form conductive pathways. When the SCGF was stretched, the conductive paths were easily destroyed resulting in a decrease in electrical conductivity. Compared with SCGF, some pores and microcracks were generated on the SSCGFs surface, and part of the Gr and CNTs were exposed on the fiber surface forming the hierarchical structure after ethyl acetate etching. When the SSCGFs were stretched or deformed, the conductive paths inside the fibers were also destroyed as for the SCGF. However, the conductive paths on the inner surfaces of the pores and microcracks could withstand large deformation without being broken as the shape of pores and the microcracks formed after etching physically changed but were not destroyed. The schematic diagram of electrically conductive paths on the surfaces of these pores and microcracks is shown in Figure 6(c). As can be seen from the figure, the V shaped conductive path transmits the current when the SSCGF based strain sensor is working. Interestingly, after suffering deformation, a V-shaped opening only becomes wider and the conductive path remains intact <span style="color:red">as can be seen from the inset SEM images.</span> This primarily contributes to enhanced electrical properties and a greater working range. Furthermore, the fillers exposed on the SSCGF surfaces after etching tended to incline and contact each other to form new conductive paths <span style="color:red">(marked with red circles in the SEM images)</span>, resulting in the strain sensing range of the fibers being greatly increased.

To demonstrate the stretching-resistance response behavior of the SSCGF, an electric circuit composed of the SSCGF-15 fiber, a light emitting diode (LED) and a power source (Keysight B2901A) was assembled. Figures 6(d)-(g) exhibit the gradual decrease in brightness of the LED as the SSCGF-15 fiber was stretched to a stretch ratio of 150%, establishing that SSCGF-15 had good conductivity and increasing electrical resistance with increasing tensile strain.
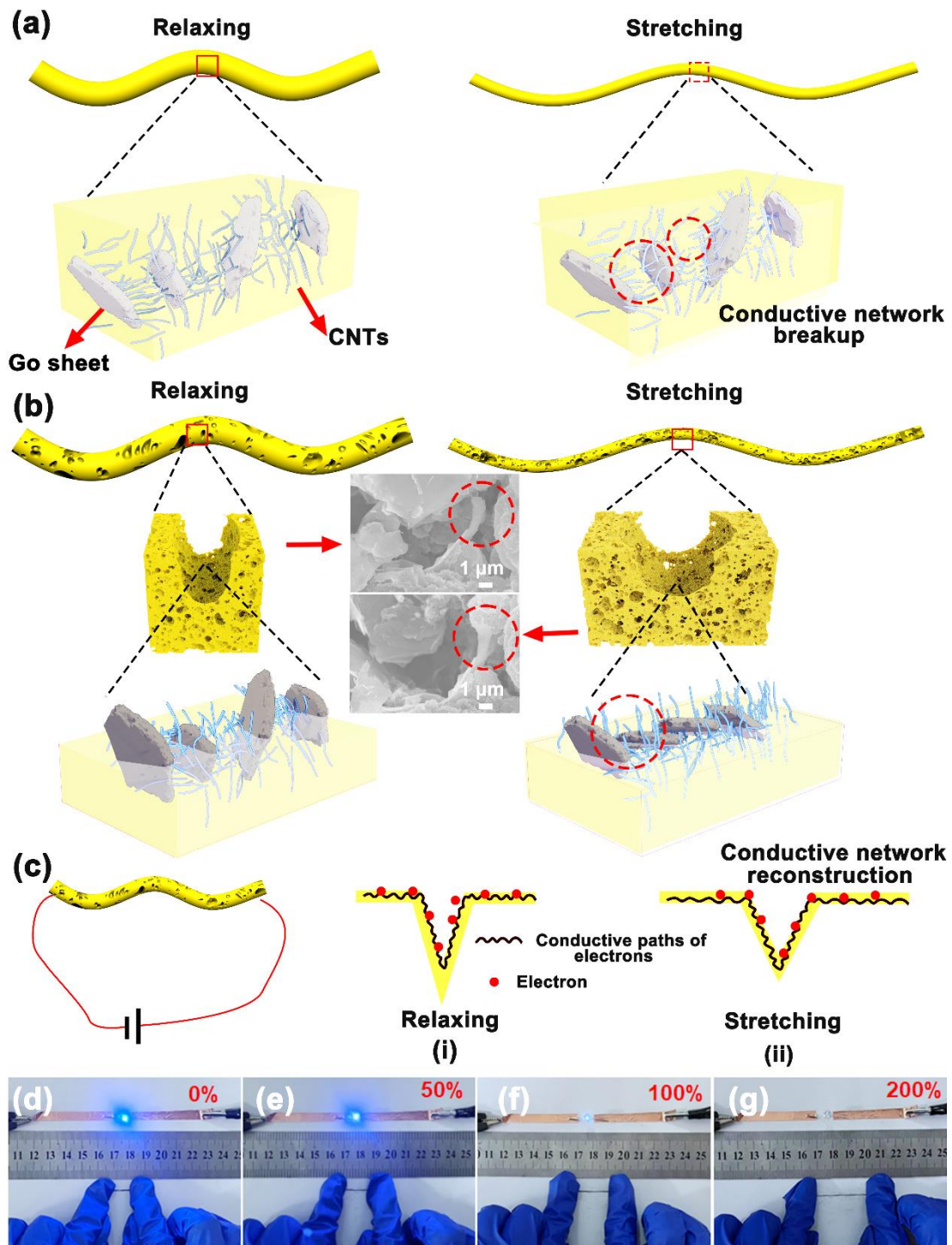
Figure 6 Schematic diagram of the conductive network formation for SCGF and SSCGF (a-c); The brightness change of a LED related to the stretching of the fiber from (d) 0% to (e) 50%; (f) 100%; (g) 200%.

To evaluate the reproducibility of the sensor materials' ability to respond and also to

determine the detection reliability of SSCGF when used in strain sensing, elastic recovery and mechanical hysteresis were investigated. The stress-strain curves during five tensile strain cycles from a zero minimum for SSCGF-15 over different strain ranges (from 0% to 50%, 100%, 150% and 200% respectively) are shown in Figure 7(a). The mechanical hysteresis of SSCGF-15 increased with the increase in the applied maximum strain in a cycle. For the same applied strain, the stress-strain curves in the loading and unloading phases did not coincide in all cycles, indicating the existence of mechanical hysteresis. This is due to the physical breakage and rearrangement of SBS molecular chains during the strain loading and unloading cycles, leading to energy dissipating and the generation of a hysteresis loop in each cycle. It can also be seen that mechanical hysteresis and stress softening of the SSCGF-15 decreased as more cycles were accumulated. The results of five consecutive cycles showed that the loading (straining) and unloading (relaxing) curves of the first loading and unloading cycle were different to the subsequent four cycles carried out at the same feed rate. For cycles one to five, each curve tended to exhibit greater set (failure to return to zero strain) than its predecessor. However, this increase in set became smaller in each successive strain cycle, suggesting that an equilibrium position can be reached when the material is used as a strain sensor. Elastic recovery in polymers is time dependent, but SSCGF has the potential to be pre-conditioned by strain cycling before it is used in specific applications. All electrical tests were carried out on the conductive fibers after undergoing five tensile loading and unloading cycles.

The I-V curves of the SSCGF-15 under strain ranges from 0% to 50%, 100%, 150% and 200% are shown in Figure 7(b). All the I-V curves for SSCGF-15 were linear, indicating an excellent electrical conductivity under various stretching conditions. Figure 7(c) shows the changes of $\Delta R/R_0$ for SSCGF-15 in 10 tensile-releasing cycles under different strain

ranges at a fixed tensile rate of 100 mm/min. As can be seen from the figure, the maximum $\Delta R/R_0$ increased slightly when the strain range changed from 0-50% to 0-100% due to the good conductivity in low strain range. When strain ranges were 0-150% and 0-200%, the maximum values of $\Delta R/R_0$ for SSCGF-15 became larger than 15000. The output $\Delta R/R_0$ maintained stable and repeatable in the whole loading-unloading process.

Figure 7(d) showed that the mechanical hysteresis for all curves decreased with increasing feed rates. In every tensile-releasing cycle group and separate tensile-release cycle, the findings and the corresponding explanation were same as that in Figure 7(a). It can also be seen from the figure that the mechanical hysteresis was minimal when the stretching speed was 1 mm/min, while it achieved the maximum at the highest stretching speed of 50 mm/min. This is mainly because the higher the tensile speed is, the harder the movement of macromolecules matches, thus greater external force is required to make the material yield, leading to the enhancement of ultimate tensile stress and mechanical hysteresis.

I-V curves of SSCGF-15 at feed rates of 1 mm/min, 5 mm/min, 10 mm/min and 50 mm/min are shown in Figure 7(e). The I-V curves for SSCGF fibers were linear for all feed rates, indicating uniform and stable electrical conductivity. Figure 7(f) shows the changes of $\Delta R/R_0$ in 10 tensile cycles of SSCGF-15 at different feed rates under a constant strain range of 0-10%. It can be seen that the maximum $\Delta R/R_0$ of SSCGF-15 increased with increasing feed rate. The peak value of $\Delta R/R_0$ varied only slightly during tensile strain cycles, indicating of the potential to have excellent stability in use. This is attributed to the formation of stable electrical conduction pathways through continuous destruction and reconstruction of Gr and CNTs conductive networks during the loading-unloading process.

In order to evaluate the durability and repeatability of the sensing capability of a SSCGF sensor, 10000 uniaxial tensile strain cycles were conducted in a constant strain range of 0-10%. The variation of $\Delta R/R_0$ with the number of cycles for SSCGF-15 is shown in Figure 7(g). As can be seen, the $\Delta R/R_0$ showed a decline in the first hundred cycles because of the continuous destruction and reconstruction of conductive pathways [43]. Thereafter the change of $\Delta R/R_0$ stabilized, showing that repeatability can be achieved in the utilization of this material by pre-conditioning it prior to use.
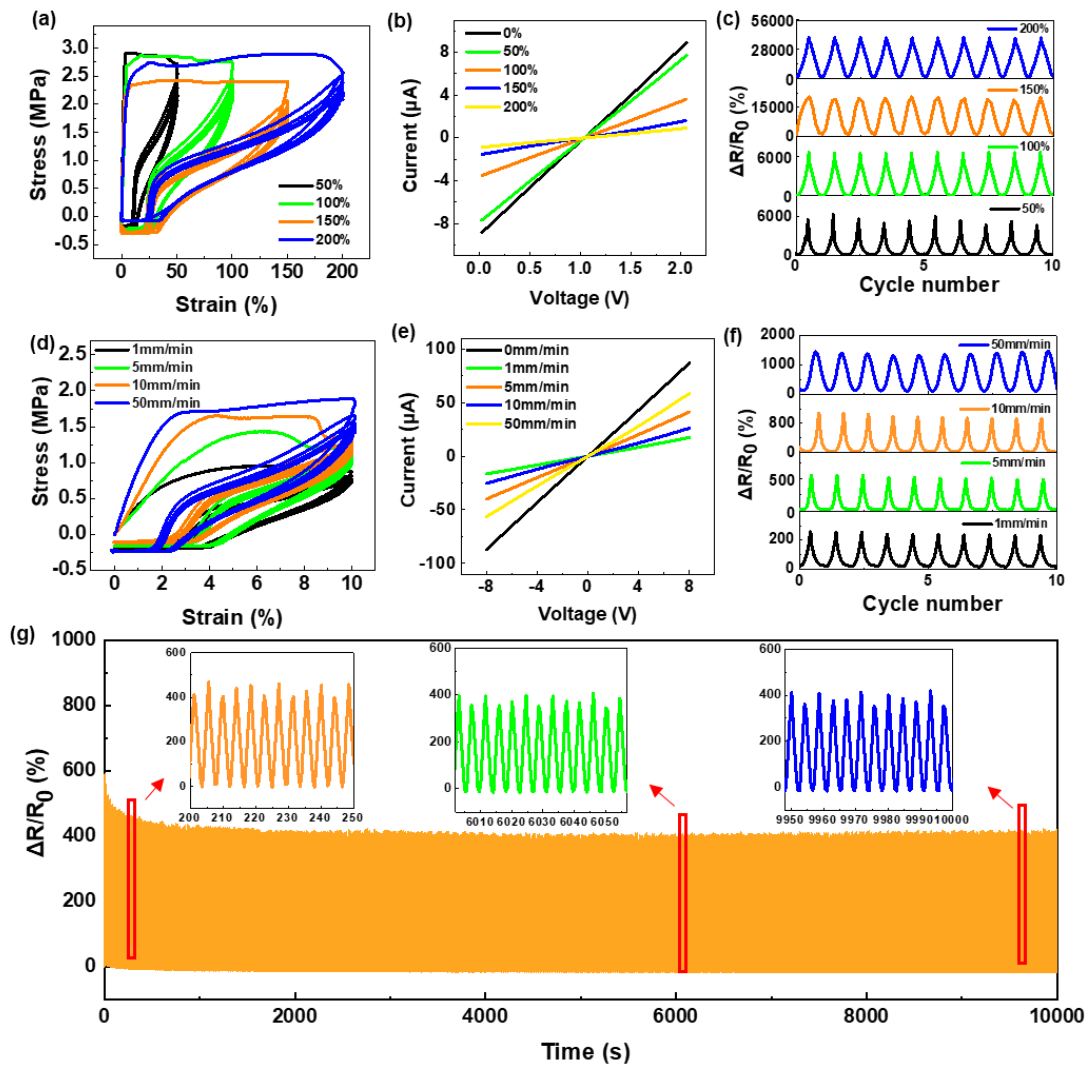


Figure 7 (a) Elastic recovery curves of SSCGF-15 in the strain ranges from 0% to 50%, 100%, 150% and 200%, respectively, feed rate was set as 10mm/min; (b) I-V curves of

SSCGF-15 under different strain ranges; (c) The dependence of relative resistance for SSCGF-15 on the cycles accumulated in the strain ranges from 0 to 50%, 100%, 150% and 200%, respectively; (d) Elastic recovery curves of SSCGF-15 in the strain range from 0 to 10% at feed rates of 1, 5, 10 and 50 mm/min, respectively; (e) I-V curves of SSCGF-15 under different feed rates; (f) The curve of $\Delta R/R_0$ versus loading-unloading cycles in the strain range from 0 to 10% for SSCGF-15 at rates of 1, 5, 10 and 50 mm/min, respectively; (g) Working durability under 10% strain for 10,000 reversible tensile strain cycles.

The feasibility of using SSCGF-15 based strain sensors in detecting human motion was investigated. A consent form was read and freely signed by the volunteer before testing. Figure 8(a) shows the relationship between the real-time relative resistance change and bending angle of interphalangeal joints. When the interphalangeal joints were bent, $\Delta R/R_0$ increased from 300% to 600%. $\Delta R/R_0$ was clearly observed to increase with the increase in angle of interphalangeal bending to 90°, indicating that the strain sensor had the ability to distinguish different degrees of bending. Figures 8(b) and (c) show the variation in $\Delta R/R_0$ on wrist bending, elbow bending and knee bending at 30°, 60° and 90°, respectively. It can be seen that $\Delta R/R_0$ increased with increased bending angles, indicating that the SSCGF based sensor was highly sensitive to changes in angle and was capable of detecting large-scale human movements.
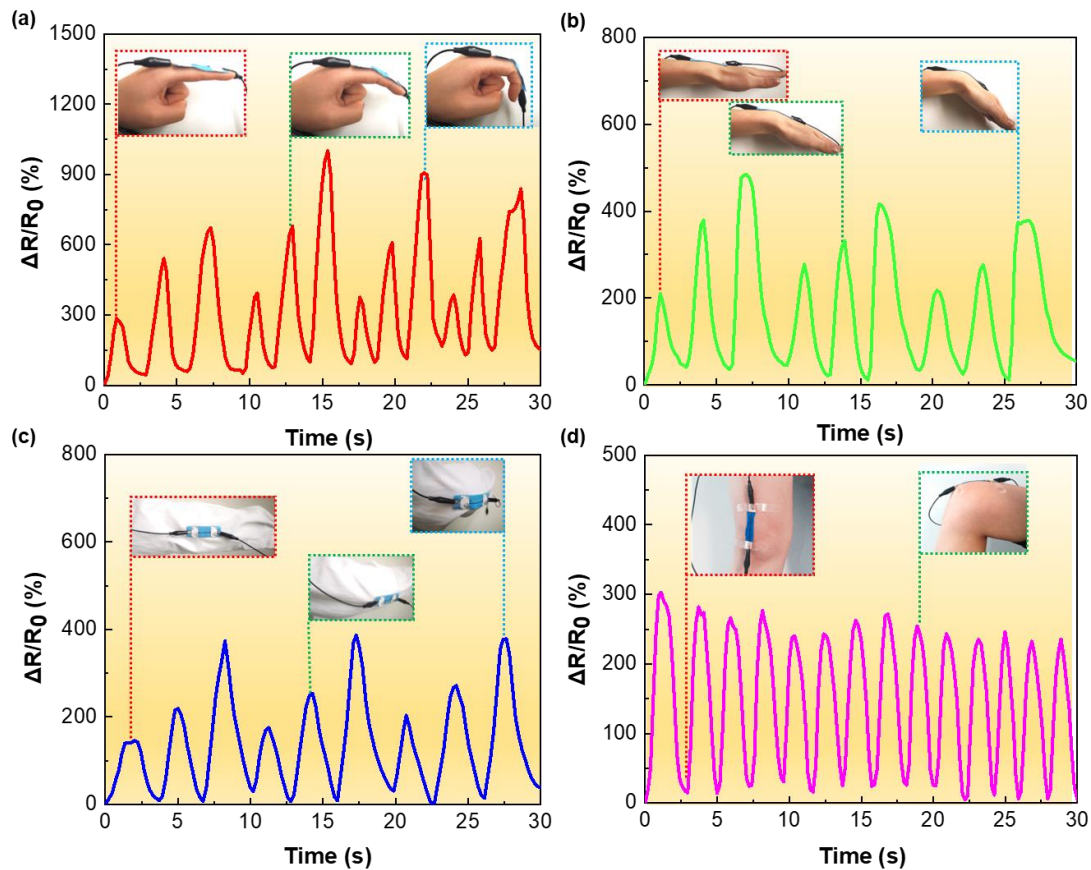
Figure 8 Application of the SSCGF-15 strain sensor in monitoring human motion at an applied voltage of 10 V. (a) Interphalangeal bending at angles of 30°, 60°, 90°; (b) Wrist bending at angles of 30°, 60°, 90°; (c) Elbow joint bending at angles of 30°, 60° and 90°; (d) Knee joint bending at 90°.

## 4. Conclusions

In this work, core-sheath structured conductive fibers of faba bean shape were prepared by a simple coaxial wet-spinning method. Solution etching was employed to reconstruct the conductive network by precipitating the conductive fillers and forming pores and microcracks. The SSCGF obtained has an enhanced electrical conductivity, a high gauge factor of 1667 and a wide working range up to 500% strain (which is about 31 times larger than the fiber possesses without etching) and maintains good durability. The SSCGF based strain sensor exhibits good sensing performance in detecting human body movements including hand joint bending (such as knuckles and wrists). This work

describes a simple way of manufacturing high-performance strain sensors that demonstrate a potential for applications in wearable electronics.

**CRediT authorship contribution statement**

**Mengsi Liu:** Writing-original draft, Investigation, Methodology. **Yaping Sheng:** Writing-original draft, Software, Data curation. **Xiaofeng Zhang:** Data curation. **Yanfen Zhou:** Funding acquisition, Writing – review & editing. **Liang Jiang:** Supervision, Writing – review & editing. **Mingwei Tian:** Methodology, Visualization. **Shaojuan Chen:** Investigation, Supervision. **Stephen Jerrams:** Writing – review & editing. **Fenglei Zhou:** Data curation, Writing – review & editing. **Jianyong Yu:** Funding acquisition, Supervision.

**Declaration of competing interest**

The authors declare that they have no known competing financial interests or personal relationships that could have appeared to influence the work reported in this paper.

**References**

[1] M. Liu, Z. Li, X. Zhao, R.J. Young, I.A. Kinloch, Fundamental Insights into Graphene Strain Sensing, Nano Letters 21(1) (2021) 833-839.

[2] Y. Xu, X. Xie, H. Huang, Y. Wang, J. Yu, Z. Hu, Encapsulated core–sheath carbon nanotube–graphene/polyurethane composite fiber for highly stable, stretchable, and sensitive strain sensor, J. Mater. Sci. 56(3) (2021) 2296-2310.

[3] D. Yang, Y. Ni, X. Kong, S. Li, X. Chen, L. Zhang, Z.L. Wang, Self-Healing and Elastic Triboelectric Nanogenerators for Muscle Motion Monitoring and Photothermal Treatment, ACS Nano 15(9) (2021) 14653-14661.

[4] D. Yang, Y. Ni, H. Su, Y. Shi, Q. Liu, X. Chen, D. He, Hybrid energy system based on solar cell and self-healing/self-cleaning triboelectric nanogenerator, Nano Energy 79 (2021) 105394.

[5] M. Amjadi, A. Pichitpajongkit, S. Lee, S. Ryu, I. Park, Highly Stretchable and Sensitive Strain Sensor Based on Silver Nanowire–Elastomer Nanocomposite, ACS Nano 8(5) (2014) 5154-5163.

[6] Y. Cai, J. Shen, G. Ge, Y. Zhang, W. Jin, W. Huang, J. Shao, J. Yang, X. Dong, Stretchable Ti3C2Tx MXene/Carbon Nanotube Composite Based Strain Sensor with Ultrahigh Sensitivity and Tunable Sensing Range, ACS Nano 12(1) (2018) 56-62.

[7] S.-H. Ha, J.-M. Kim, Highly sensitive and stretchable strain sensor based on self-aligned and periodic cracking of wavy metal nanowire/elastomer composite film, Smart. Mater. Struct. 30(6) (2021) 065022.

[8] Z. Han, L. Liu, J. Zhang, Q. Han, K. Wang, H. Song, Z. Wang, Z. Jiao, S. Niu, L. Ren, High-performance flexible strain sensor with bio-inspired crack arrays, Nanoscale 10(32) (2018) 15178-15186.

[9] Y. He, D. Wu, M. Zhou, Y. Zheng, T. Wang, C. Lu, L. Zhang, H. Liu, C. Liu, Wearable Strain Sensors Based on a Porous Polydimethylsiloxane Hybrid with Carbon Nanotubes and Graphene, ACS. Appl. Mater. Inter. 13(13) (2021) 15572-15583.

[10] J.-H. Lee, J. Kim, D. Liu, F. Guo, X. Shen, Q. Zheng, S. Jeon, J.-K. Kim, Highly Aligned, Anisotropic Carbon Nanofiber Films for Multidirectional Strain Sensors with Exceptional Selectivity, Adv. Funct. Mater. 29(29) (2019) 1901623.

[11] Z. Liu, Y. Zheng, L. Jin, K. Chen, H. Zhai, Q. Huang, Z. Chen, Y. Yi, M. Umar, L.

Xu, G. Li, Q. Song, P. Yue, Y. Li, Z. Zheng, Highly Breathable and Stretchable Strain Sensors with Insensitive Response to Pressure and Bending, Adv. Funct. Mater. 31(14) (2021) 2007622.

[12] H. Yang, X. Xiao, Z. Li, K. Li, N. Cheng, S. Li, J.H. Low, L. Jing, X. Fu, S. Achavananthadith, F. Low, Q. Wang, P.-L. Yeh, H. Ren, J.S. Ho, C.-H. Yeow, P.-Y. Chen, Wireless Ti3C2Tx MXene Strain Sensor with Ultrahigh Sensitivity and Designated Working Windows for Soft Exoskeletons, ACS Nano 14(9) (2020) 11860-11875.

[13] R. Zhang, S. Li, C. Ying, Z. Hu, A. Lv, H. Hu, X. Fu, S. Hu, Q. Liu, C.-P. Wong, Bioinspired design of flexible strain sensor with high performance based on gradient filler distributions, Compos. Sci. Technol. 200 (2020) 108319.

[14] Q. Chen, Y. Li, D. Xiang, Y. Zheng, W. Zhu, C. Zhao, H. Li, H. Han, Y. Shen, Enhanced Strain Sensing Performance of Polymer/Carbon Nanotube-Coated Spandex Fibers via Noncovalent Interactions, Macromol. Mater. Eng. 305(2) (2020) 1900525.

[15] Q. Chen, D. Xiang, L. Wang, Y. Tang, E. Harkin-Jones, C. Zhao, Y. Li, Facile fabrication and performance of robust polymer/carbon nanotube coated spandex fibers for strain sensing, Compos. Part. A-appl. S. 112 (2018) 186-196.

[16] D. Xiang, X. Zhang, E. Harkin-Jones, W. Zhu, Z. Zhou, Y. Shen, Y. Li, C. Zhao, P. Wang, Synergistic effects of hybrid conductive nanofillers on the performance of 3D printed highly elastic strain sensors, Compos. Part. A-appl. S. 129 (2020) 105730.

[17] C. Lee, L. Jug, E. Meng, High strain biocompatible polydimethylsiloxane-based conductive graphene and multiwalled carbon nanotube nanocomposite strain sensors, Appl. Phys. Lett. 102(18) (2013) 183511.

[18] C.-J. Lee, K.H. Park, C.J. Han, M.S. Oh, B. You, Y.-S. Kim, J.-W. Kim, Crack-induced Ag nanowire networks for transparent, stretchable, and highly sensitive strain sensors, Sci. Pep-uk. 7(1) (2017) 7959.

[19] H. Jeon, S.K. Hong, M.S. Kim, S.J. Cho, G. Lim, Omni-Purpose Stretchable Strain Sensor Based on a Highly Dense Nanocracking Structure for Whole-Body Motion Monitoring, Appl. Mater. Inter. 9(48) (2017) 41712-41721.

[20] D. Xiang, X. Zhang, Y. Li, E. Harkin-Jones, Y. Zheng, L. Wang, C. Zhao, P. Wang, Enhanced performance of 3D printed highly elastic strain sensors of carbon nanotube/thermoplastic polyurethane nanocomposites via non-covalent interactions, Compos. Part B-Eng. 176 (2019) 107250.

[21] Y. Lin, S. Liu, S. Chen, Y. Wei, X. Dong, L. Liu, A highly stretchable and sensitive strain sensor based on graphene–elastomer composites with a novel double-interconnected network, J. Mater. Chem. C. 4(26) (2016) 6345-6352.

[22] C. Luo, B. Tian, Q. Liu, Y. Feng, W. Wu, One-Step-Printed, Highly Sensitive, Textile-Based, Tunable Performance Strain Sensors for Human Motion Detection, J. Mater. Chem. C. 5(2) (2020) 1900925.

[23] M. Nie, Y.-h. Xia, H.-s. Yang, A flexible and highly sensitive graphene-based strain sensor for structural health monitoring, Cluster. Comput. 22(4) (2019) 8217-8224.

[24] S. Ryu, P. Lee, J.B. Chou, R. Xu, R. Zhao, A.J. Hart, S.-G. Kim, Extremely Elastic Wearable Carbon Nanotube Fiber Strain Sensor for Monitoring of Human Motion, ACS Nano 9(6) (2015) 5929-5936.

[25] Y. Wu, I. Karakurt, L. Beker, Y. Kubota, R. Xu, K.Y. Ho, S. Zhao, J. Zhong, M. Zhang, X. Wang, L. Lin, Piezoresistive stretchable strain sensors with human machine interface demonstrations, Sensor. Actuat. A-Phys. 279 (2018) 46-52.

[26] X. Zhang, D. Xiang, Y. Wu, E. Harkin-Jones, J. Shen, Y. Ye, W. Tan, J. Wang, P. Wang, C. Zhao, Y. Li, High-performance flexible strain sensors based on biaxially stretched conductive polymer composites with carbon nanotubes immobilized on reduced graphene oxide, Compos. Part. A-appl. S. 151 (2021) 106665.

[27] X. Zhang, D. Xiang, W. Zhu, Y. Zheng, E. Harkin-Jones, P. Wang, C. Zhao, H. Li, B. Wang, Y. Li, Flexible and high-performance piezoresistive strain sensors based on carbon nanoparticles@polyurethane sponges, Compos. Sci. Technol. 200 (2020) 108437.

[28] H. Zhou, Z. Jin, Y. Yuan, G. Zhang, W. Zhao, X. Jin, A. Ma, H. Liu, W. Chen, Self-repairing flexible strain sensors based on nanocomposite hydrogels for whole-body monitoring, Colloid. Surface. A. 592 (2020) 124587.

[29] J. Huang, J. Zhou, Y. Luo, G. Yan, Y. Liu, Y. Shen, Y. Xu, H. Li, L. Yan, G. Zhang, Y. Fu, H. Duan, Wrinkle-Enabled Highly Stretchable Strain Sensors for Wide-Range Health Monitoring with a Big Data Cloud Platform, Acs. Appl. Mater. Inter. 12(38) (2020) 43009-43017.

[30] D.N. Matveev, V.P. Vasilevskii, I.L. Borisov, V.V. Volkov, A.V. Volkov, Effects of Dry-Jet Wet Spinning Parameters on Properties of Polysulfone Hollow Fiber Membranes, Russ. J. Appl. Chem+. 93(4) (2020) 554-563.

[31] S. Wu, S. Peng, Y. Yu, C.-H. Wang, Strategies for Designing Stretchable Strain Sensors and Conductors, Russ. J. Appl. Chem+. 5(2) (2020) 1900908.

[32] G. Mohammadkhani, S. Kumar Ramamoorthy, K.H. Adolfsson, A. Mahboubi, M. Hakkarainen, A. Zamani, New Solvent and Coagulating Agent for Development of Chitosan Fibers by Wet Spinning, Polymers 13(13) (2021) 2121.

[33] X. Shen, Q. Hu, M. Ge, Fabrication and characterization of multi stimuli-responsive fibers via wet-spinning process, Spectrochim. Acta. A. 250 (2021) 119245.

[34] S. Seyedin, S. Uzun, A. Levitt, B. Anasori, G. Dion, Y. Gogotsi, J.M. Razal, MXene Composite and Coaxial Fibers with High Stretchability and Conductivity for Wearable Strain Sensing Textiles, Adv. Funct. Mater. 30(12) (2020) 1910504.

[35] S. Chun, Y. Choi, W. Park, All-graphene strain sensor on soft substrate, Carbon

116 (2017) 753-759.

[36] C. Tan, Z. Dong, Y. Li, H. Zhao, X. Huang, Z. Zhou, J.-W. Jiang, Y.-Z. Long, P. Jiang, T.-Y. Zhang, B. Sun, A high performance wearable strain sensor with advanced thermal management for motion monitoring, Nat. Commun. 11(1) (2020) 3530.

[37] B. Jin, J. Liu, Y. Shi, G. Chen, Q. Zhao, S. Yang, Solvent-Assisted 4D Programming and Reprogramming of Liquid Crystalline Organogels, Adv. Mater. 34(5) (2022) 2107855.

[38] Y. Wang, J. Fu, Q. Song, J. Yu, Y. Wang, Z. Hu, Regulating the dissolving system of ultra-high molecular weight polyethylene to enhance the high-strength and high-modulus properties of resultant fibers, J. Appl. Polym. Sci. 139(29) (2022) e52653.

[39] M. Al Aiti, A. Das, M. Kanerva, M. Järventausta, P. Johansson, C. Scheffler, M. Göbel, D. Jehnichen, H. Brünig, L. Wulff, S. Boye, K. Arnhold, J. Kuusipalo, G. Heinrich, Dry-Jet Wet Spinning of Thermally Stable Lignin-Textile Grade Polyacrylonitrile Fibers Regenerated from Chloride-Based Ionic Liquids Compounds, Materials 13(17) (2020).

[40] D. Bao, L. Liu, T. Sun, Y. Han, F. Meng, M. Zhao, Y. Yu, J. Guo, S. Zhang, Solid solid phase change (SSPC) chitosan-g-mPEG fiber with improved mechanical performance via in-situ wet spinning process, Carbohyd. Polym. 240 (2020) 116313.

[41] W. Eom, H. Shin, R. Amabde, S. Lee, K. Lee, D. Kang, T.H. Han, Large-scale wet-spinning of highly electroconductive MXene fibers, Nat. Commun. 11 (2020) 2825.

[42] D. Kang, P.V. Pikhitsa, Y.W. Choi, C. Lee, S.S. Shin, L. Piao, B. Park, K.-Y. Suh, T.-i. Kim, M. Choi, Ultrasensitive mechanical crack-based sensor inspired by the spider sensory system, Nature 516(7530) (2014) 222-226.

[43] K. Tian, Q. Pan, H. Deng, Q. Fu, Shear induced formation and destruction behavior of conductive networks in nickel/polyurethane composites during strain sensing,

Compos. Part. A-appl. S. 130 (2020) 105757.